J Solid State Electrochem (2011) 15:115–123
DOI 10.1007/s10008-010-1072-2

ORIGINAL PAPER

A mathematical model of nanoparticulate mixed oxide pseudocapacitors; part II: the effects of intrinsic factors

Hossein Farsi · Fereydoon Gobal

Received: 30 April 2008 / Revised: 1 April 2010 / Accepted: 6 April 2010 / Published online: 27 April 2010

Abstract Our previously reported mathematical model for a mixed oxide nanoparticulate-based supercapacitor containing $RuO_2{\cdot}xH_2O$ and $MO_2{\cdot}yH_2O$ (M being another suitable transition metal) was analyzed. Both double-layer and faradaic processes responsible for charge/discharge were considered. The effects of the intrinsic factors, unit cell length, state of charge, and the exchange current densities of the electrochemical processes of the constituents on the performance of the model supercapacitor were clarified. Compensation effects where each constituent compensates the shortcomings of the other at specific conditions of discharge are analyzed in the light of the model.

Keywords Pseudocapacitors · Nanoparticles · Metal oxide · Ragone plot · Discharge curve · State of charge

Nomenclature

E	Local electrode potential, V
E_0	Initial local electrode potential, V
$\overline{E}$	Dimensionless local electrode potential, E/E_0
h_{Ru}	Length of crystal lattice on the $RuO_2{\cdot}xH_2O$ surface, cm
h_M	Length of crystal lattice on the $MO_2{\cdot}yH_2O$ surface, cm
$i_{0,Ru}$	Exchange current density for the faradaic reaction of $RuO_2{\cdot}xH_2O$, A cm^{-2}
$i_{0,M}$	Exchange current density for the faradaic reaction of $MO_2{\cdot}yH_2O$, A cm^{-2}
i_C	Double-layer current per unit volume of electrode, A cm^{-3}
i_{cell}	Cell current density, A cm^{-2}
i_f	Faradaic current per unit volume of electrode, A cm^{-3}
$\overline{i}_C$	Dimensionless double-layer current, $i_C L/i_{cell}$
$\overline{i}_f$	Dimensionless faradaic current, $i_f L/i_{cell}$
L	Thickness of the electrode, cm
S_V	Specific surface area per unit volume of the electrode, cm^2/cm^3
t	Time, s
t_d	Discharge time, s
V_0	Initial potential before charge, 0.5 V (vs. SCE)
x	Position coordinate, cm
X_M	Volume fraction of $MO_2{\cdot}yH_2O$ in the electrode

Greek

δ_{Ru}	State of charge of $RuO_2{\cdot}xH_2O$
δ_M	State of charge of $MO_2{\cdot}yH_2O$
Φ_{cell}	Cell potential or the matrix potential difference between the two current collectors, V
$\overline{\Phi}_{cell}$	Dimensionless cell potential, $\frac{\Phi_{cell}}{2V_0}$
θ	Fraction of oxidized species in the faradaic reaction
ξ	Dimensionless position coordinate, x/L

Introduction

In the first part of this work, we developed a mathematical model of mixed oxide nanoparticulate-based pseudocapacitors containing of RuO_2 and MO_2, which is a metal oxide

This paper has been presented in International Battery Materials Association (IBA) 2007 Conference, Shenzhen, China.

H. Farsi (✉)
Department of Chemistry, University of Birjand,
P.O. Box: 97175-615, Birjand, Iran
e-mail: hofarsi@birjand.ac.ir

F. Gobal
Department of Chemistry, Sharif University of Technology,
P.O. Box: 11365-9516, Tehran, Iran
e-mail: gobal@sharif.edu

that is stable chemically and shows a capacitive behavior on the potential range of ruthenium oxide's stability, by considering both double-layer (DL) charge/discharge and faradaic processes [1]. Also, we have already categorized the factors influencing the performance of pseudocapacitors into three categories: synthesis factors like particle size or pore size distribution and electrode composition, intrinsic factors like exchange current densities of the relevant electrochemical processes and unit cell length, and operating factors like withdrawing cell current and temperature [2, 3]. The effect of particle size and electrode composition was investigated in the previous part. Briefly, we showed that by increasing the particle size or the content of larger particles, both DL and faradaic currents diminish because specific surface area decreases. Therefore, particle size distribution affects both the power and energy densities and consequently the pseudocapacitor's performance.

In this part, we analyze our model considering the influence of intrinsic factors containing of unit cell length, state of charge (SOC), and exchange current density of metal oxide on the performance of pseudocapacitors. Our last experience in theoretical analysis of the performance of a model nanoparticulate supercapacitor [2] showed that both energy density and power density increase by decreasing in unit cell length because of enhancing in the number of active sites per unit of surface area. Also, increasing in exchange current density as a kinetics parameter exhibits a complex discharge time-dependent behavior.

Another intrinsic factor could be the state of charge. The phrase state of charge is routinely used to discuss the performance of the electrochemical energy devices, defined as the ratio of the available capacity of a cell to its maximum attainable capacity [4–6]. In fact, it is a measure of the amount of the available electrical energy [7, 8], i.e., the state of charge of an electrical energy storage device is necessary information in its operation. The user will know exactly the amount of power that the energy storage device is capable of providing if the state of charge can be estimated accurately [9]. Precise SOC estimation of the power of an energy storage device can avoid unpredicted system interruption and prevent the rechargeable electrical system from being overcharged and overdischarged, which may cause permanent damage to their internal structure [10, 11]. Unfortunately, SOC cannot be measured directly but must be estimated based on measurable parameters such as current and voltage. So far, several methods have been developed to estimate SOC such as the coulomb counting method [10, 12, 13], techniques employing Kalman filter [14–16], impedance measurements [4, 8, 17, 18], and so on. Although the term state of charge are widely used for discussing the performance of both batteries and supercapacitors, a noticeable difference between them is that the state of charge for a supercapacitor depends to the potential against of batteries [19–23]. Also, in the case of lithium intercalated electrode, the amount of lithium present inside the electrode (inserted lithium) is a direct measure of the state of charge of the battery [24, 25]. Lin et al. [26] have used the same approach to relate the state of charge to the amount of hydrogen inserted into the ruthenium oxide by using experimental data of Jow and Zheng [27] who calculated the transferred charge on the interface, Q, as a result of hydrogen insertion into hydrated ruthenium oxide electrode which is a function of potential from the cyclic voltammogram using:

$$Q(V) = \int_{v_0}^{v} \frac{i}{s}\, dV \tag{1}$$

where i is current, s is voltage scan rate, V is potential, and v_0 and v are initial and final potential in cyclic voltammograms, respectively. Then the hydrogen content of ruthenium oxide, δ, in the following faradaic reaction:

$$RuO_2 \cdot xH_2O + \delta H^+ + \delta e \rightleftarrows H_\delta RuO_2 \cdot xH_2O \tag{2}$$

was calculated by the following equation:

$$\delta(V) = \frac{Q(V)}{\frac{m}{M}F} \tag{3}$$

where m is the weight of the active materials, M is the molecular weight of hydrated ruthenium oxide, and F is Faraday's constant. Lin et al. [26] called δ as state of charge which is seems a reasonable nomenclature due to directly dependency of capacitance to the charge via $C = \frac{Q}{V}$. In fact, $\frac{m}{M}F$ shows maximum attainable charge if all of ruthenium oxide molecules participate in faradaic redox reaction. It is expectable that the capacitance and consequently the performance of a supercapacitor increase by raising the state of charge, i.e., the same effect which will be observed by decreasing the unit cell length. Due to this, in the present work, we have used the $\frac{\delta}{h^2}$ ratio to examine the effects of both unit cell length and state of charge together.

Materials and methods

The effects of "state of charge" and unit cell length

Our model considers an electrochemical adsorption or absorption process of H^+ ion on or into the mixed metal oxides matrix as a faradaic process which is responsible for pseudocapacitance [1]. Thus, the transferred charge or capacitance of mixed metal oxides relates to the number of H^+ ions which are adsorbed/absorbed or inserted electrochemically per each molecule of metal oxides or simply the state of charge. It has been shown experimen-

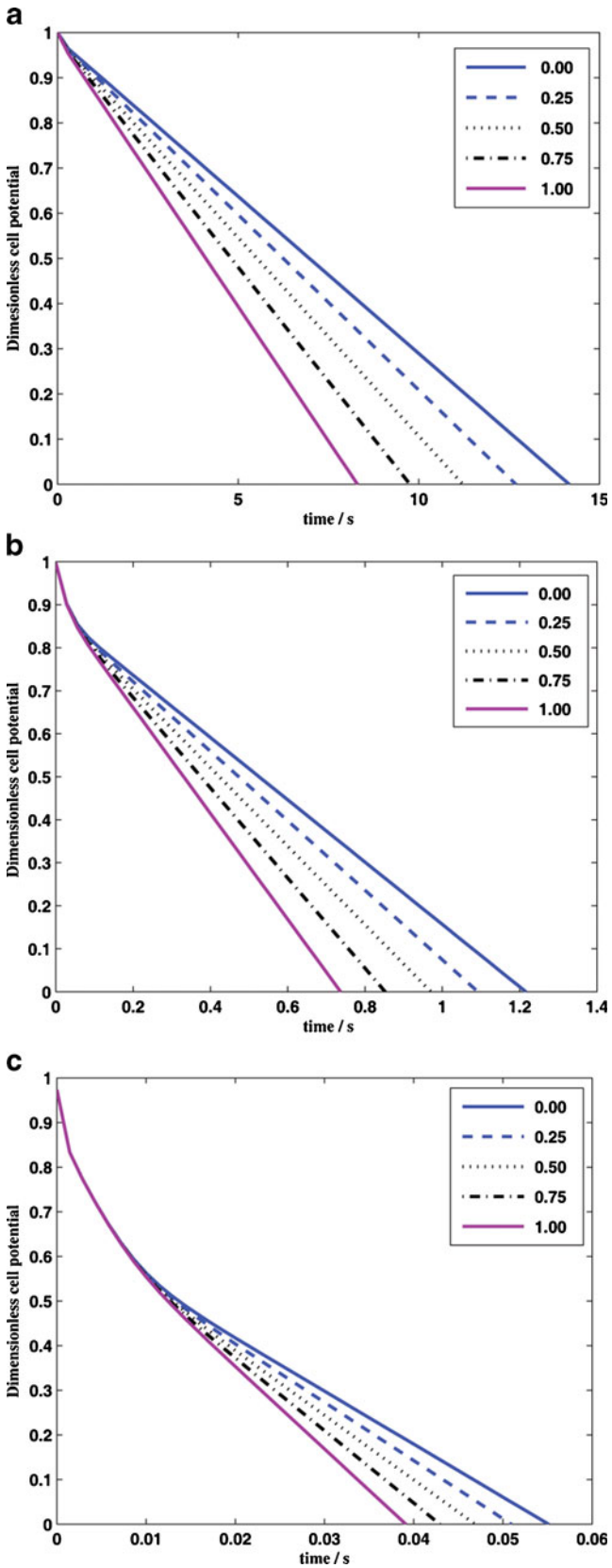

Fig. 1 Discharge curves for a set of pseudocapacitors consisting of 15 nm $RuO_2{\cdot}xH_2O$ and $MO_2{\cdot}yH_2O$ nanoparticles with $i_{0,M} = i_{0,Ru} = 1 \times 10^{-5}$ A cm^{-2} and $\frac{\delta_M}{h_M^2} = 0.5\frac{\delta_{Ru}}{h_{Ru}^2}$=1.56×10^{14} cm^{-2} at **a** 0.05, **b** 0.5, and **c** 5 A cm^{-2}. The legend's values show the volume fractions of $MO_2{\cdot}yH_2O$ nanoparticles, X_M

tally that one H^+ ion adsorbs/inserts on two molecular units of $RuO_2{\cdot}xH_2O$, or the "state of charge", δ_{Ru}, is 0.5 [26]. Unfortunately, such experimental results are not available for other metal oxides but because of higher capacity of $RuO_2{\cdot}xH_2O$ compared to other metal oxides, a smaller state of charge is expectable for them, i.e., δ_M<0.5. Also, at the same surface area by increasing in the number of active sites the charge transferred to the unit of surface area will increase, too. This implies that the smaller the unit cell length, h, the higher the transferred charge and so the capacitance. Therefore, smaller unit cells implies (parallels) higher densities of the state of charge (meaning that unit area of the surface simply accommodates higher multiples of δ), and so we investigate the $\frac{\delta}{h^2}$ ratio effect instead of the influences of δ and h, separately. We expect that $\frac{\delta_M}{h_M^2} < \frac{\delta_{Ru}}{h_{Ru}^2}$, so in this stage of our analysis, we consider $\frac{\delta_M}{h_M^2} = 0.5\frac{\delta_{Ru}}{h_{Ru}^2}$ while the sizes and the exchange current densities for nanoparticles of $RuO_2{\cdot}xH_2O$ and $MO_2{\cdot}yH_2O$ are kept the same. The numerical parameters are the same as the ones used in our previous work [1] except for the particle's sizes that in this work are assumed to be 15 nm for both metal oxides.

The effects of exchange current density

To investigate the effects of exchange current density as a dominant factor and a kinetics parameter on the performance of the mixed oxide pseudocapacitor, we have considered two cases: $i_{0,M} > i_{0,Ru}$ and $i_{0,M} < i_{0,Ru}$, and assuming $\frac{\delta_M}{h_M^2} = 0.5\frac{\delta_{Ru}}{h_{Ru}^2}$ and the same particle size of 15 nm for both metal oxides. Our previous experience [2] in the analysis of Lin's Model [26] tells us that the effects of decreasing exchange current density are in parallel with the effects of increasing unit cell length. Therefore, because of $\frac{\delta_M}{h_M^2} = 0.5\frac{\delta_{Ru}}{h_{Ru}^2}$, if $i_{0,M} < i_{0,Ru}$, a more dramatic decrease on the performance of a mixed oxide is conceivable. This means that $MO_2{\cdot}yH_2O$ not only possesses less active sites per unit area but also has a lower rate of charge transfer to the particle's surface compared to $RuO_2{\cdot}xH_2O$. In the present work, we assume $i_{0,Ru} = 1 \times 10^{-5} Acm^{-2}$ and $i_{0,M} = 1 \times 10^{-4} Acm^{-2}$.

Results and discussion

The effects of "state of charge" and unit cell length

Figure 1a–c depicts the galvanostatic discharge behaviors of a set of mixed oxide pseudocapacitors having different

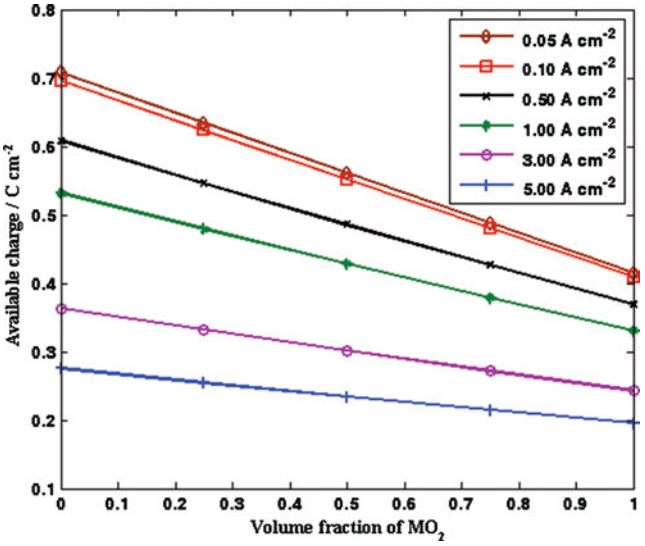

Fig. 2 Available charge, $i_{cell} \times t$, vs. volume fraction of $MO_2{\cdot}yH_2O$ particles in a composite electrode for a set of pseudocapacitors consisting of 15 nm $RuO_2{\cdot}xH_2O$ and $MO_2{\cdot}yH_2O$ nanoparticles with $i_{0,M} = i_{0,Ru} = 1 \times 10^{-5}$ A cm^{-2} and $\frac{\delta_M}{h_M^2} = 0.5\frac{\delta_{Ru}}{h_{Ru}^2}$=1.56×10^{14} cm^{-2}. The legend's values show the cell current densities

compositions of 15 nm-sized nanoparticles of $RuO_2{\cdot}xH_2O$ and $MO_2{\cdot}yH_2O$ with $\frac{\delta_M}{h_M^2} = 0.5\frac{\delta_{Ru}}{h_{Ru}^2}$ and $i_{0,Ru} = i_{0,M} = 1 \times 10^{-5} Acm^{-2}$ at different withdrawing cell currents. As these figures show, by increasing the content of $MO_2{\cdot}yH_2O$, the discharge time diminishes. Also, in a given X_M, volume fraction of $MO_2{\cdot}yH_2O$, the discharge time decreases with rising of the withdrawing cell current, too. Obviously, surface area does not vary by changing of X_M because of the same sizes of both $RuO_2{\cdot}xH_2O$ and $MO_2{\cdot}yH_2O$ nanoparticles. Although the surface area is fixed, the number of active sites reduces with X_M, and less charge will be stored at the interface, and obviously, this small charge requires a short time to discharge. Also, for a given capacitor with a finite stored charge, increasing the withdrawing cell current causes a shorter discharge time. Another feature in these curves is the cell potential drop in the early stages of discharge, which increases by both i_{cell} and X_M. According to Lin [26] and also our previous work [2], this has two origins: Ohmic drop and kinetics resistance. Clearly, cell's potential drop increases with i_{cell} due to Ohm's law, but the reason for potential drop with X_M in a given cell current should be the kinetic resistance of faradaic reaction. By increasing X_M, the number of active sites (adsorptive sites)

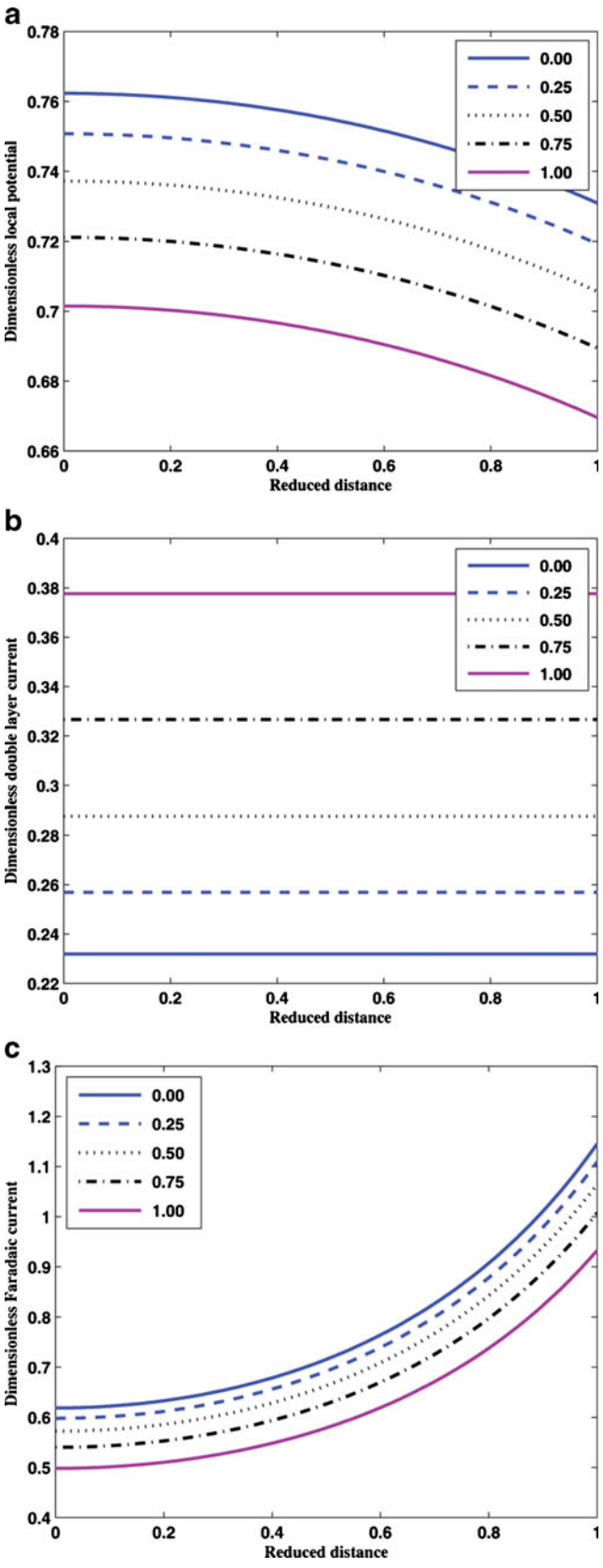

Fig. 3 Distribution of **a** dimensionless local potential, **b** dimensionless DL current, and **c** dimensionless faradaic current inside the positive electrode for a set of pseudocapacitors consisting of 15 nm $RuO_2{\cdot}xH_2O$ and $MO_2{\cdot}yH_2O$ nanoparticles with $i_{0,M} = i_{0,Ru} = 1 \times 10^{-5}$ A cm^{-2} and $\frac{\delta_M}{h_M^2} = 0.5\frac{\delta_{Ru}}{h_{Ru}^2}$=1.56×10^{14} cm^{-2} at i_{cell}=2.5 A cm^{-2} and t_d=0.06 s. The legend's values show the volume fractions of $MO_2{\cdot}yH_2O$ nanoparticles, X_M

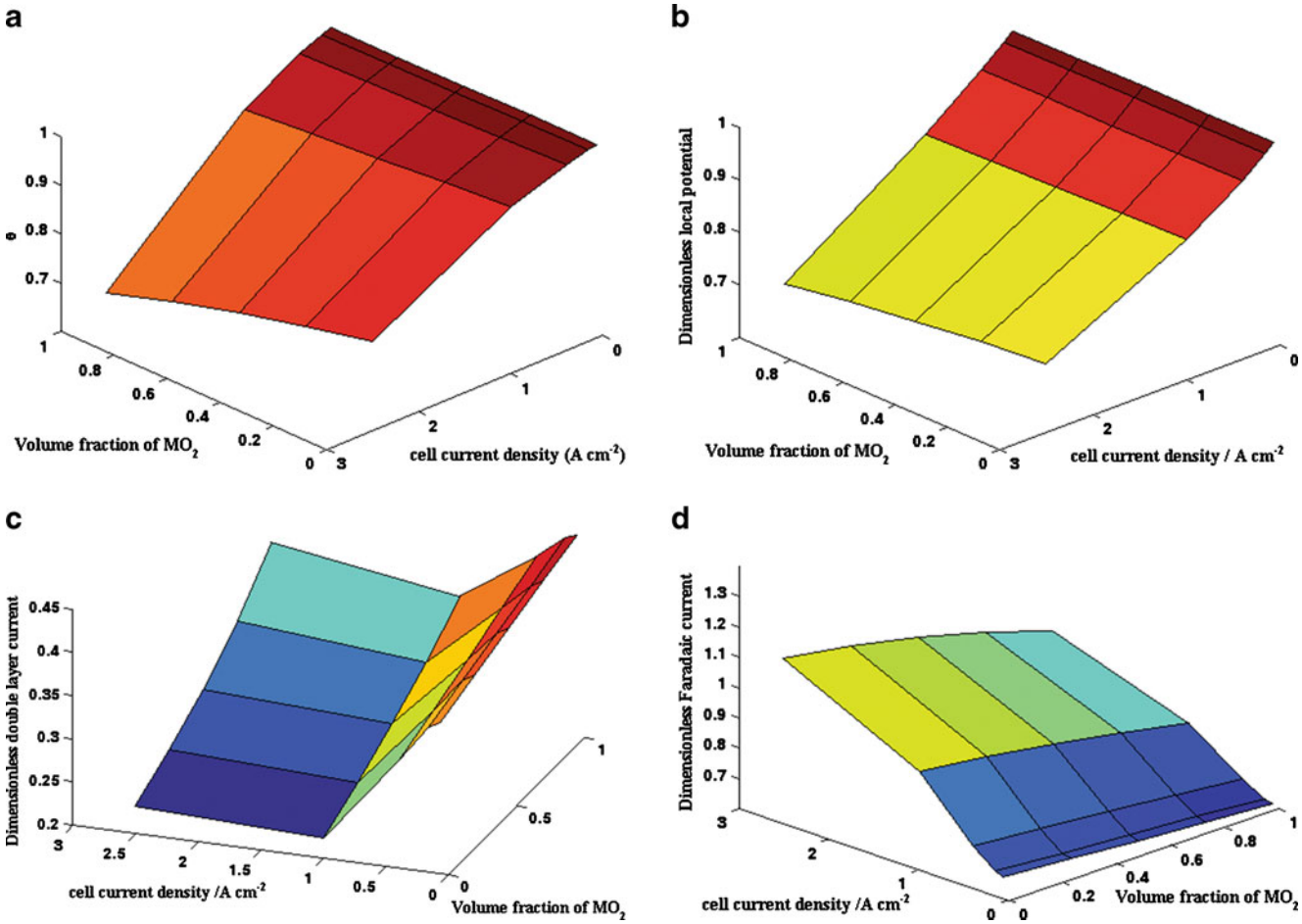

Fig. 4 **a** Surface coverage, **b** dimensionless local potential, **c** dimensionless DL current, and **d** dimensionless faradaic current profiles on the surface of positive electrode for a set of pseudocapacitors consisting of 15 nm $RuO_2{\cdot}xH_2O$ and $MO_2{\cdot}yH_2O$ nanoparticles with $i_{0,M} = i_{0,Ru} = 1 \times 10^{-5}$ A cm^{-2}, $\frac{\delta_M}{h_M^2} = 0.5\frac{\delta_{Ru}}{h_{Ru}^2} = 1.56 \times 10^{14}$ cm^{-2} and t_d=0.06 s at different cell current densities and X_M. The legend's values show the volume fractions of $MO_2{\cdot}yH_2O$ nanoparticles, X_M

diminishes, and therefore, less charge will be available to the surface faradaic reaction. Consequently, the kinetic resistance will increase. These findings are illustrated and amplified through plots of available charge, $i_{cell} \times t$, vs. X_M at different withdrawing cell currents, Fig. 2.

To investigate how dimensionless local potential, double-layer, and faradaic currents inside the electrode change during discharge, these quantities were plotted against reduced distance at a discharge time of 0.06 s, cell current density of 2.5 A, and at different electrode compositions. The results have been displayed in Fig. 3a–c. Dimensionless local potential decreases by going from current collector to the electrode surface where the surface faradaic reaction takes place (Fig. 3a). There is no uniform distribution in local potential because at a short discharge time, not all the active sites can get involved in the faradaic processes. On the other hand, local potential have smaller values in larger contents of $MO_2{\cdot}yH_2O$ because a pseudocapacitor with a larger X_M has a smaller number of active sites, and so a larger fraction of active sites need to be engaged in the reaction which implies a smaller local potential. Figure 3b depicts the profile of double-layer discharge current inside the positive electrode. At the first glance, it appears as a homogeneous distribution because in this case, discharge time is larger than double-layer charging time constant. Another feature of this plot is the increasing of double-layer current with X_M. As discussed previously [1, 2], two factors are important in controlling double-layer charge/discharge current; specific surface area, S_V, and $\frac{\partial E}{\partial t}$. In this special case, S_V does not change with X_M because of the same particle sizes for both metal oxides. Therefore, $\frac{\partial E}{\partial t}$ governs the double-layer current, and a pseudocapacitor with a sharper local potential drop vs. time will have a larger double-layer current. From Fig. 3a and our discussion, it is clear that in the given discharge time, a larger content of $MO_2{\cdot}yH_2O$ produces a higher double-layer current. Figure 3c presents the faradaic current distribution inside the positive electrode. An ascendant

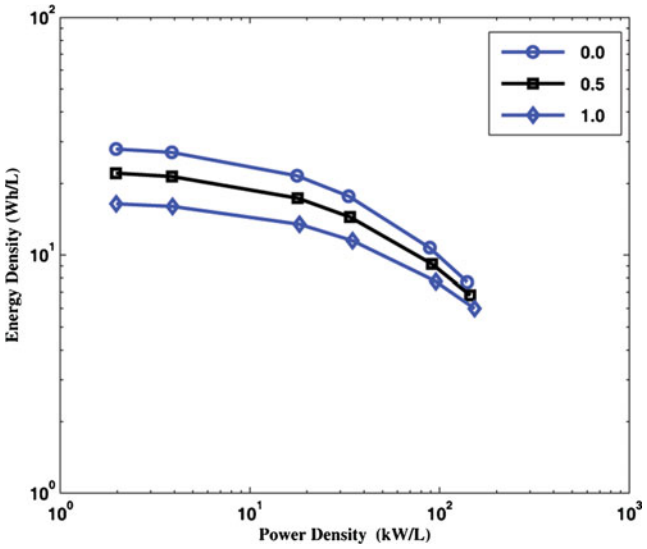

Fig. 5 Ragone plots for a three pseudocapacitors consisting of 15 nm $RuO_2{\cdot}xH_2O$ and $MO_2{\cdot}yH_2O$ nanoparticles with $i_{0,M} = i_{0,Ru} = 1 \times 10^{-5}$ A cm^{-2} and $\frac{\delta_M}{h_M^2} = 0.5\frac{\delta_{Ru}}{h_{Ru}^2}$=1.56×10^{14} cm^{-2} and different volume fractions of $MO_2{\cdot}yH_2O$ nanoparticles, X_M, which have been shown in the legend

hyperbolic behavior by going from current collector to the electrode surface is observed. This is due to the exponential dependency of $\frac{\partial^2\overline{E}}{\partial\xi^2}$ to $\overline{E}$ via faradaic current with a Butler–Volmer behavior. Therefore, a pseudocapacitor with a larger $\overline{E}$ is expected [1].

Using the three dimensional graphs, we have presented the effects of volume fractions of $MO_2{\cdot}yH_2O$ and withdrawing cell current on the fraction of oxidized species, θ, dimensionless local potential, $\overline{E}$, Fig. 4a, b. Also, the variation of dimensionless double-layer and faradaic currents upon the mentioned variables are presented in Fig. 4c, d. For all of these quantities, the same behavior is observed by changing X_M at constant cell current which can be accounted for on the base of the above discussion on their distributions inside the electrode material. However, θ and $\overline{E}$ decrease by increasing cell current at constant X_M because more active sites will be involved in charge transfer process at a constant discharge time (Fig. 4a, b). Regarding the double-layer and faradaic currents, at cell's currents smaller than 1 A, a compensation effect is observed. At small withdrawing cell current, the faster process (double-layer discharging) fulfills the supply of this current, and by increasing the cell current, the contribution of faradaic current amplifies (Fig. 4c, d). The total energy harvested in time t_d and power densities were calculated for all simulated capacitors, and their profiles are shown at volume fractions of 0, 0.5, and 1 of $MO_2{\cdot}yH_2O$ through the Ragone plots in Fig. 5. As this figure shows, energy density decreases by increasing X_M. Energy density is proportional to the charge passing through the interface, and this charge

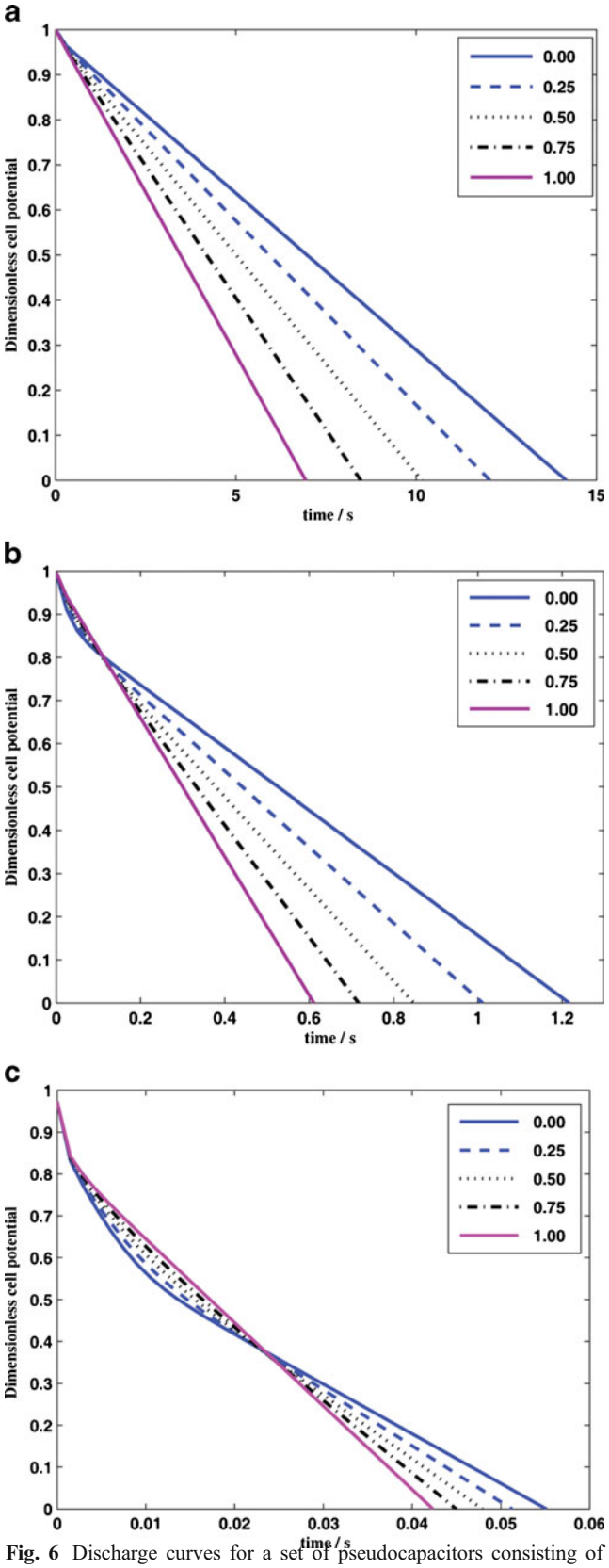

Fig. 6 Discharge curves for a set of pseudocapacitors consisting of 15 nm $RuO_2{\cdot}xH_2O$ and $MO_2{\cdot}yH_2O$ nanoparticles with $i_{0,M} = 10 \times i_{0,Ru} = 1 \times 10^{-4}$ A cm^{-2} and $\frac{\delta_M}{h_M^2} = 0.5\frac{\delta_{Ru}}{h_{Ru}^2}$=1.56×10^{14} cm^{-2} at **a** 0.05, **b** 0.5, and **c** 5 A cm^{-2}. The legend's values show the volume fractions of $MO_2{\cdot}yH_2O$ nanoparticles, X_M

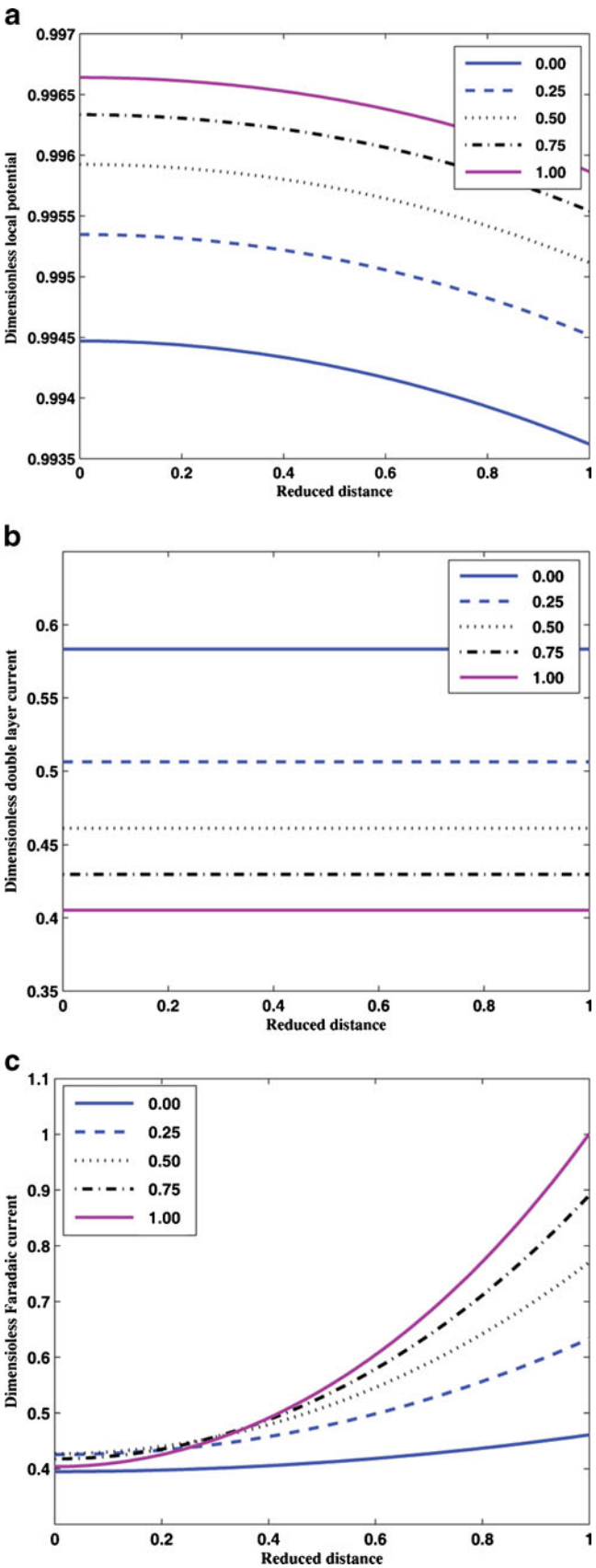

Fig. 7 Distribution of **a** dimensionless local potential, **b** dimensionless DL current, and **c** dimensionless faradaic current inside the positive electrode for a set of pseudocapacitors consisting of 15 nm $RuO_2{\cdot}xH_2O$ and $MO_2{\cdot}yH_2O$ nanoparticles with $i_{0,M} = 10 \times i_{0,Ru} = 1 \times 10^{-4}$ A cm^{-2} and $\frac{\delta_M}{h_M^+} = 0.5\frac{\delta_{Ru}}{h_{Ru}^+} = 1.56 \times 10^{14}$ cm^{-2} at i_{cell}=0.06 A cm^{-2} and t_d=0.03 s. The legend's values show the volume fractions of $MO_2{\cdot}yH_2O$ nanoparticles, X_M

itself manifests the number of active sites at the interface. Therefore, the higher the number of active sites, the larger the transferred charge and consequently the larger the energy density. While power density increases slowly by volume fraction of $MO_2{\cdot}yH_2O$, both the energy and power density tend to enhance by increasing cell current. Incidentally, the energy density depends on t_d as well, which itself decreases as X_M is raised.

The effects of exchange current density

Figure 6a–c shows the galvanostatic discharge curves for a set of mixed oxide supercapacitors which contain both $RuO_2{\cdot}yH_2O$ and $MO_2{\cdot}yH_2O$ with different ratios, the same particle size of 15 nm, and measured at different withdrawing cell currents. The feature these discharge curves have in common with the previous ones is the decreasing of discharge time by increasing the withdrawing cell current which we have already interpreted in details. On the other hand, the discharge curves cross each other at a special discharge time which depends on the withdrawing cell current, i.e., a smaller crossing time is witnessed at a larger cell current. To account for the findings, it should be pointed out that the kinetic resistance has two origins: rate of supply of charge to the interface which depends on the amount of stored charge and the exchange current density of faradaic reaction and rate of charge consumption at the interface which depends on withdrawing cell current. In the present case, although $MO_2{\cdot}yH_2O$ has a smaller surface density of charge compared to $RuO_2{\cdot}xH_2O$, it is better capable of providing the charge at interface because its processes have a higher exchange current density compared to $RuO_2{\cdot}xH_2O$. The observed discharge behavior (Fig. 6a–c) gives us good information about the conditions where a factor is dominant. These curves indicate clearly that at the final stages of discharge process, the exchange current density is not important, and a pseudocapacitor with a smaller X_M has a larger discharge time because of the more stored charge whereas at initial stages of discharge, a pseudocapacitor with a larger contribution of $MO_2{\cdot}yH_2O$ shows a larger discharge time. Apparently, there is a compensation effect between these metal oxides. At earlier stages of discharging, a metal oxide (here $MO_2{\cdot}yH_2O$) with larger exchange current density is responsible for providing the requested charge, and at final stages of discharge, a metal oxide with a better capability of

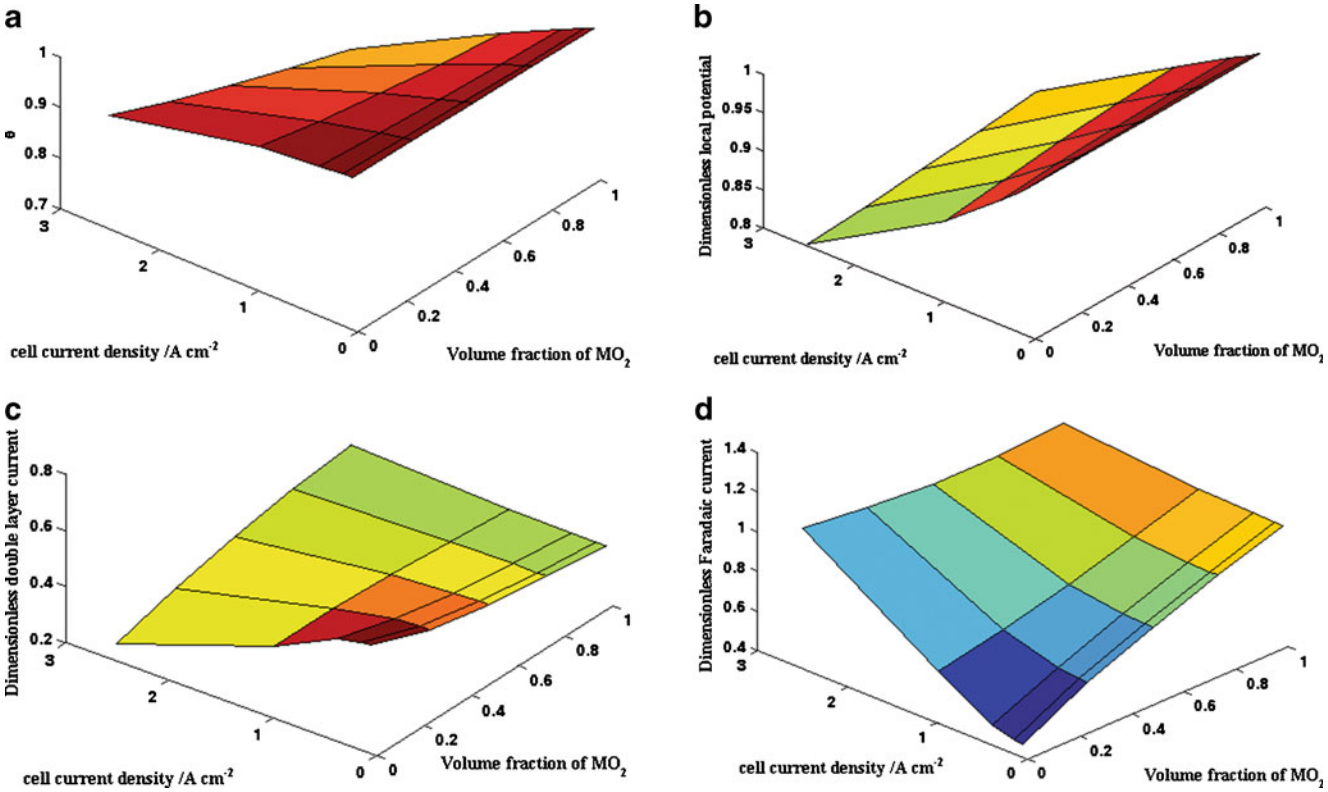

Fig. 8 **a** Surface coverage, **b** dimensionless local potential, **c** dimensionless DL current, and **d** dimensionless faradaic current profiles on the surface of positive electrode for a set of pseudocapacitors consisting of 15 nm $RuO_2{\cdot}xH_2O$ and $MO_2{\cdot}yH_2O$ nanoparticles with $i_{0,M} = 10 \times i_{0,Ru} = 1 \times 10^{-4}$ A cm^{-2} and $\frac{\delta_M}{h_M^2} = 0.5\frac{\delta_{Ru}}{h_{Ru}^2} = 1.56 \times 10^{14}$ cm^{-2} and t_d=0.06 s at different cell current densities and X_M. The legend's values show the volume fractions of $MO_2{\cdot}yH_2O$ nanoparticles, X_M

charge storage (here $RuO_2{\cdot}xH_2O$) governs the capacitive behavior.

To study how potential and currents change inside the positive electrode, we have plotted the values of dimensionless local potential, double-layer, and faradaic currents against reduced distance at a discharge time of 0.03 s, when the exchange current density is the dominant factor, Fig. 7a–c. Figure 7a depicts descending profiles of dimensionless local potential going from current collector to the surface of mixed metal oxides matrix where the electrode is exposed to the electrolyte, and the surface faradaic reaction takes place for all values of X_M. Also larger contents of $MO_2{\cdot}yH_2O$ cause a larger potential in the entire bulk of electrode. In this small discharge time, the dominant factor is the kinetics parameter, i.e., exchange current density. This implies that the charge demanded by the withdrawing cell current must be preferentially supplied by the faradaic reaction of $MO_2{\cdot}yH_2O$. Therefore, a drop in dimensionless local potential is observed by increasing X_M. The profile of double-layer discharge current, Fig. 7b, confirms that small values of $\overline{E}$ (which is a consequence of large and negative values of $\frac{\partial E}{\partial t}$ and small X_M values) exhibit large double-layer current. Figure 7c depicts the faradaic current distribution inside the electrode. As before, it shows an exponential ascent behavior due to dependency of faradaic current to $\overline{E}$. The simultaneous effects of X_M and i_{cell} on θ, $\overline{E}$, double-layer and faradaic currents have been illustrated by 3D presentations in Fig. 8a–d, respectively. Again, θ and $\overline{E}$ behave as expected. Also, the above

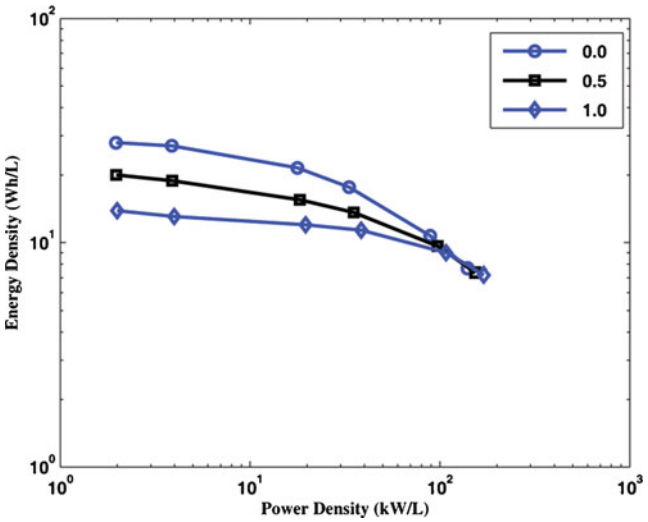

Fig. 9 Ragone plots for a three pseudocapacitors consisting of 15 nm $RuO_2{\cdot}xH_2O$ and $MO_2{\cdot}yH_2O$ nanoparticles with $i_{0,M} = 10 \times i_{0,Ru} = 1 \times 10^{-4}$ A cm^{-2} and $\frac{\delta_M}{h_M^2} = 0.5\frac{\delta_{Ru}}{h_{Ru}^2} = 1.56 \times 10^{14}$ cm^{-2} and different volume fractions of $MO_2{\cdot}yH_2O$ nanoparticles, X_M, which have been shown in the legend

discussion about double-layer and faradaic current distributions is usable to interpret the behaviors of these quantities on the electrode surface. The compensation effect for double-layer and faradaic currents at small withdrawing cell current is observed. However, at larger cell currents, this behavior is not witnessed as the electrochemical process is not fast enough and cannot provide such large currents.

Finally, Fig. 9 shows Ragone plots of three mixed oxide pseudocapacitors with different contents of $MO_2{\cdot}yH_2O$. At small cell currents (small power densities), smaller X_M causes higher energy density because at small withdrawing cell currents, rate of charge consumption is smaller than its production, and thus, the more the stored charge, the higher the energy density. Consequently, pure $RuO_2{\cdot}xH_2O$-based pseudocapacitor has the maximum energy density. At large withdrawing cell currents (high power densities), all stored charge is consumed, and a capacitor with a faster charge production capability (based on $MO_2{\cdot}yH_2O$) will have a higher energy density. Therefore, it is expected that the Ragone plots of these pseudocapacitors approach each other at high power densities. This has indeed been witnessed in Fig. 9.

Conclusion

In this part of work, our developed model [1] for a nanoparticulate mixed oxide pseudocapacitor which considers both double-layer charging/discharging and faradaic process for both metal oxides was analyzed to study the effects of intrinsic factors; surface density of charge, and exchange current density. The results for surface density of charge effects were interpreted in terms of the active site number per unit area and the number of hydrogen ions which adsorb on. The effects of exchange current density as a kinetics parameter was discussed in terms of competition between the rate of charge produced at the interface via the faradaic processes and rate of charge-consuming process (withdrawing cell current). Our studies showed the existing helpfulness between $RuO_2{\cdot}xH_2O$ and $MO_2{\cdot}yH_2O$, i.e., at the earlier stage of discharging, $MO_2{\cdot}yH_2O$ assists $RuO_2{\cdot}xH_2O$ to supply the demanded charge. Finally, we have applied a simple model to describe the pseudocapacity, its origin, and its influencing factor.

References

1. Farsi H, Gobal F (2009) J Solid State Electrochem 13:433
2. Farsi H, Gobal F (2007) J Solid State Electrochem 11:1085
3. Farsi H, Gobal F (2007) Comput Mater Sci 39:678
4. Rodrigues S, Munichandraiah N, Shukla AK (2000) J Power Sources 87:12
5. Blood PJ, Sotiropoulos S (2002) J Power Sources 110:96
6. Pop V, Bergveld HJ, Notten PHL, Op het Veld JHG, Regtien PPL (2009) Measurement 42:1131
7. Milocco RH, Castro BE (2009) J Power Sources 194:55
8. Zhongxue L, Jie C (2008) Microelectron Eng 85:1549
9. Tseng CY, Lin CF (2005) J Power Sources 147:282
10. Ng KS, Mooa CS, Chen YP, Hsieh YC (2009) Appl Energy 86:1506
11. Lee S, Kim J, Lee J, Cho BH (2008) J Power Sources 185:1367
12. Çadirci Y, Özkazanc Y (2004) J Power Sources 129:330
13. Hansen T, Wang CJ (2005) J Power Sources 141:351
14. Plett GL (2004) J Power Sources 134:252
15. Plett GL (2004) J Power Sources 134:262
16. Plett GL (2004) J Power Sources 134:277
17. Hammouche A, Karden E, De Doncker RW (2004) J Power Sources 127:105
18. Blanke H, Bohlen O, Buller S, Doncker RW, Fricke B, Hammouche A, Linzen D, Thele M, Sauer DU (2005) J Power Sources 144:418
19. Conway BE (1991) J Electrochem Soc 138:1539
20. Conway BE, Pell WG (2003) J Solid State Electrochem 7:637
21. Conway BE, Briss V, Wojtowicz J (1997) J Power Sources 66:1
22. Pell WG, Conway BE (1996) J Power Sources 63:255
23. Mahon PJ, Paul GL, Keshishian SM, Vassallo AM (2000) J Power Sources 91:68
24. Wakihara M, Yamamoto O (Eds) (1998) Lithium ion batteries—fundamentals and performance. Wiley–VCH, Weinheim
25. Shriram S, Renganathan NG, Ganesan M, Dhananjeyan MVT (2005) J Electroanal Chem 576:43
26. Lin C, Ritter JA, Popov BN, White RE (1999) J Electrochem Soc 146:3168
27. Jow TR, Zheng JP (1998) J Electrochem Soc 145:49